PERGAMON

International Journal of Heat and Mass Transfer 44 (2001) 1485–1493

International Journal of HEAT and MASS TRANSFER

www.elsevier.com/locate/ijhmt

Numerical simulation of thermal fluid instability between two horizontal parallel plates

Hongxing Yang [a,*], Zuojin Zhu [b], John Gilleard [a]

[a] *Department of Building Services Engineering, The Hong Kong Polytechnic University, Hung Hom, Kowloon, Hong Kong*
[b] *Department of Thermal Science and Energy Engineering, University of Science and Technology of China, Anhui, Hefei 230026, People's Republic of China*

Received 19 July 1999; received in revised form 14 June 2000

Abstract

The buoyancy-induced thermal fluid instability between two parallel horizontal plates has been investigated numerically by solving the governing equations of base and perturbation fields using a fractional algorithm, in which the fourth-order Adams scheme and the Bi-CGSTAB scheme are embedded. An initial assumption of the perturbed temperature was made by a Gaussian random number generator. A primitive static fluid with Prandtl number 0.73 was induced to flow in the gap between the two horizontal parallel plates for three different cases: top heating, bottom heating and heating from both plates. The kinetic energy of induced flow in each vertical section and in the whole domain was calculated. The results can demonstrate whether the thermal fluid flow is stable or unstable. A linear decaying behavior is found after the initial stage. The total fluid kinetic energy in the domain converges for the top heating case, but diverges for the other two heating cases.

1. Introduction

Buoyancy-induced convection between two parallel plates is a classical problem [1]. However, despite its apparent simplicity, the detailed heat transfer mechanism and fluid flow patterns are still worthy of careful study. The investigation on thermal fluid instability was raised when research on natural ventilation in buildings was carried out.

To date, a large amount of works have been devoted to this heat transfer phenomenon. One early piece of work on laminar natural convection in plate wall channel was undertaken [2]. However, the majority of research on natural convection has been reported since the early 1980s. For the purpose of understanding flow patterns and heat transfer near a wall, a theoretical analysis of vortex instability over horizontal and inclined heated surfaces was reported by Chen and Tzuoo [3]. They illustrated the neutral stability curves by solving an eigenvalue problem derived from the governing equations of perturbation quantities with the base flow. They also indicated that the base flow is governed by the two-dimensional steady boundary layer equations in pseudo-similarity coordinates, which can be solved by the Runge–Kutta integration scheme. These stability curves were compared with experimental results and approximate analysis without considering the effect of a streamwise pressure gradient term. It was found that, for small angles of inclination ($0^\circ < \phi < 30^\circ$), there is a new vortex instability, and for large angles of inclination ($30^\circ < \phi \leqslant 90^\circ$), more accurate results than before have been obtained.

Yousef et al. [4] reported the experimental results of free convection from an upward-facing isothermal horizontal surface to obtain the physical nature of the boundary layer flow. Surprisingly, they found that the periodic flow instability effects were substantially important. The flow instability induced large, random changes in local and average Nusselt number, which underscored the under-stable nature of the flow over a horizontal heated surface. The boundary layer is separated from the plate at a distance, which is independent of the plate size and temperature. The natural convection

* Corresponding author. Tel.: +852-2766-5863; fax: +852-2774-6146.
E-mail address: behxyang@polyu.edu.hk (H. Yang).

0017-9310/01/$ - see front matter
PII: S0017-9310(00)00214-3

Nomenclature

a_1, a_2	real number for pressure matrix
b_1, b_2	real number for pressure matrix
C_p	specific heat at constant pressure (J/kg K)
E_{px}	non-dimensional kinetic energy integration over a vertical section
E_{ov}	non-dimensional kinetic energy integration over the whole domain
g	gravitational acceleration (m/s^2)
H	gap height (m)
$\vec{i}$	unit vector in x direction
$\vec{j}$	unit vector in y direction
k	thermal conductivity (W/m K)
L	gap length (m)
n	unit normal vector of a boundary surface
p	pressure (Pa)
p_∞	ambient pressure (Pa)
Pr	Prandtl number
Ra	Rayleigh number
Ra_{av}	average Rayleigh number
S	gap ratio defined by H/L
u	velocity component in x direction (m/s)
u_0	velocity scale (m/s)
v	velocity component in y direction (m/s)

Greek symbols

β_T	coefficient of fluid thermal expansion (l/K)
δ_t	non-dimensional time interval
ΔT_w	temperature difference $(T_w - T_\infty)$ K
Θ	non-dimensional temperature
w	wall
ρ	density (kg/m^3)
∇^2	Laplacian operator

Superscripts

n	time level
l	iteration level

Subscripts

b	base
p	perturbation
x	x direction
ov	overall
∞	ambient

in a plate wall channel is not quite similar to the case of a single plate, but the physical nature of heat transfer near a wall is the same.

Narusawa and Suzukawa [5] performed an experimental study on double-diffusive cellular convection due to a uniform lateral heat flux. Takao et al. [6] later conducted a numerical study of this type of convection, and found that heating induced distortion of the stable vertical gradient. This in turn produced roll cells that developed into a series of layers growing laterally from the heated boundary. Under a uniform heat flux, the principal non-dimensional parameter governing the stability of double diffusive convection is the same for both the narrow slot problem and a semi-infinite body of fluid.

Experimental results on natural convection in divergent, convergent and parallel vertical channels show that the flow pattern in a divergent channel is significantly different from that in a convergent channel [7]. For divergent channels, there is a re-circulation loop occupying the remainder of the cross-section in which the central portion is a down flow and the outer portion is an up flow. On the other hand, in the convergent channels, the flow is only an up flow.

Azevedo and Sparrow [2] studied the natural convection in an open-ended inclined channel by experiments with water. It was found that the secondary flow in the form of longitudinal vortices existed above a threshold Rayleigh number for bottom heating only. However, only two different inclinations (30° and 45°) were used to obtain the effect of a gravitational field.

Recently, a great deal of numerical work on natural convection has been reported. A literature review on the three-dimensional flow was reported by Vafai and Ettefagh [8]. A numerical scheme based on Galerkin's method of finite element formulation, in which the relevant linear systems are solved by the conjugate residual (CR) algorithm and the conjugate gradient square (CGS) algorithm, has been utilized by Iyer and Vafai [9] to simulate the natural convection in a cylindrical annular with multiple perturbations on the inner and outer cylinders. Iyer and Vafai illustrated that the presence of multiple perturbations on the inner and outer cylinders leads to a 50% increase in the overall heat transfer rate, compared with the regular annular without any perturbation. An explicit projection method has been used by Lin and Lin [10] to investigate numerically the buoyancy-induced vortex flow and heat transfer in a mixed convective flow through a heated duct with slight duct inclination. It was found that if the opposing-buoyancy force is high enough, a slender reverse-flow zone occurs in the duct core and a generation of vortex rolls exists in the entry region.

This study examines the natural convection and thermal instability for the two-dimensional flow between two parallel horizontal plates. The geometry and temperature boundary conditions are illustrated in Fig. 1. The open-ended parallel plates have a gap height H and length L. The fluid with Prandtl number 0.73 between the two plates is heated by three different heating modes: top plate heating, bottom plate heating and heating from both plates. The two faces are open to the en-

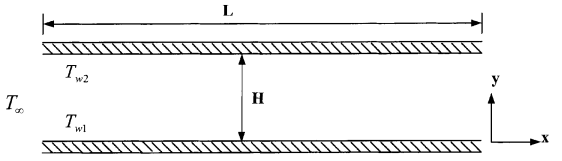

Fig. 1. Schematic diagram of the open-ended channel between two parallel horizontal plates.

vironment with a constant temperature T_∞ and pressure P_∞. Results have been obtained under two-dimensional unsteady laminar conditions for the base and perturbation fields at Rayleigh numbers covering the range from 2.87×10^3 to 9.11×10^4. The Boussinesq approximation and constant thermal dynamical property assumptions are applied to simplify the governing equations. A fourth-order integration scheme and Bi-CGSTAB algorithm for linear systems are used in the simulation work. Thermal-fluid instability and the time evolution of local and average Nusselt numbers have received special attention.

2. The mathematical model

Natural convection in the channel can be described by the following equations:

$$\frac{\partial \rho}{\partial t}+\frac{\partial \rho u}{\partial x}+\frac{\partial \rho v}{\partial y}=0, \tag{1}$$

$$\frac{\partial \rho u}{\partial t}+\frac{\partial \rho uu}{\partial x}+\frac{\partial \rho vu}{\partial y}=-\frac{\partial p}{\partial x}+\frac{\partial}{\partial x}\left(\mu\frac{\partial u}{\partial x}\right)+\frac{\partial}{\partial y}\left(\mu\frac{\partial u}{\partial y}\right), \tag{2}$$

$$\frac{\partial \rho v}{\partial t}+\frac{\partial \rho uv}{\partial x}+\frac{\partial \rho vv}{\partial y}=-\frac{\partial p}{\partial y}-\rho g+\frac{\partial}{\partial x}\left(\mu\frac{\partial v}{\partial x}\right)+\frac{\partial}{\partial y}\left(\mu\frac{\partial v}{\partial y}\right), \tag{3}$$

$$\frac{\partial \rho C_\mathrm{p} T}{\partial t}+\frac{\partial \rho u C_\mathrm{p} T}{\partial x}+\frac{\partial \rho v C_\mathrm{p} T}{\partial y}=\frac{\partial}{\partial x}\left(k\frac{\partial C_\mathrm{p} T}{\partial x}\right)+\frac{\partial}{\partial y}\left(k\frac{\partial C_\mathrm{p} T}{\partial y}\right). \tag{4}$$

Assuming that the fluid has constant properties, in addition to Boussinesq assumption, one obtains the non-dimensionalized governing equations as follows:

$$\frac{\partial u}{\partial x}+\frac{\partial v}{\partial y}=0, \tag{5}$$

$$\frac{\partial u}{\partial t}+\frac{\partial uu}{\partial x}+\frac{\partial vu}{\partial y}=-\frac{\partial p}{\partial x}+\left(\frac{Pr}{Ra}\right)^{\frac{1}{2}}\left(\frac{\partial^2 u}{\partial x^2}+\frac{\partial^2 u}{\partial y^2}\right), \tag{6}$$

$$\frac{\partial u}{\partial t}+\frac{\partial uv}{\partial x}+\frac{\partial vv}{\partial y}=-\frac{\partial p}{\partial y}+\Theta+\left(\frac{Pr}{Ra}\right)^{\frac{1}{2}}\left(\frac{\partial^2 v}{\partial x^2}+\frac{\partial^2 v}{\partial y^2}\right), \tag{7}$$

$$\frac{\partial \Theta}{\partial t}+\frac{\partial u\Theta}{\partial x}+\frac{\partial v\Theta}{\partial y}=\frac{1}{\sqrt{RaPr}}\left(\frac{\partial^2 \Theta}{\partial x^2}+\frac{\partial^2 \Theta}{\partial y^2}\right). \tag{8}$$

For convenience, the over-bars have been dropped, where the Prandtl number Pr is accompanied by the Rayleigh number $Ra = g\beta_\mathrm{T}(T_\mathrm{w} - T_\infty)H/v\alpha$. In addition, g and T_∞ are the gravitational acceleration and ambient temperature, and T_w and β_T are the wall temperature and thermal-expansion coefficient of fluid. The following dimensionless parameters are used:

$$\bar{u}=\frac{u}{u_0};\ \bar{v}=\frac{v}{u_0};\ \bar{t}=\frac{tu_0}{H};\ \bar{x}=\frac{x}{H};\ \bar{y}=\frac{y}{H};\quad \bar{p}=\frac{p}{\rho_\infty u_0^2};\ \Theta=\frac{T-T_\infty}{T_\mathrm{w}-T_\infty}, \tag{9}$$

where $u_0 = \sqrt{g\beta_\mathrm{T}(T_\mathrm{w} - T_\infty)H}$ and H are the velocity and length scale, respectively.

Let $\Theta = \Theta_\mathrm{b} + \Theta_\mathrm{p}$ be decomposed into the base and perturbed temperature with subscript b and p, respectively. Assume that the gap ratio $S = H/L$ is small without any regard of the penetration effects of ambient fluid from the open-ended sides. Assuming the base temperature to be independent of the horizontal coordinate, the base temperature is governed by

$$\frac{\partial \Theta_\mathrm{b}}{\partial t}=\frac{1}{\sqrt{RaPr}}\frac{\partial^2 \Theta_\mathrm{b}}{\partial y^2}, \tag{10}$$

while the perturbed temperature Θ_p is governed by

$$\frac{\partial \Theta_\mathrm{p}}{\partial t}+\frac{\partial u\Theta_\mathrm{p}}{\partial x}+\frac{\partial v\Theta_\mathrm{b}}{\partial y}+\frac{\partial v\Theta_\mathrm{p}}{\partial y}=\frac{1}{\sqrt{RaPr}}\left(\frac{\partial^2 \Theta_x}{\partial x^2}+\frac{\partial^2 \Theta_\mathrm{p}}{\partial y^2}\right). \tag{11}$$

The boundary conditions for the base field are

$$\Theta_\mathrm{b}(t,0)=\begin{cases}0 & \text{for top heating,}\\ 1 & \text{for bottom heating,}\\ 1 & \text{for heating from both plates,}\end{cases} \tag{12}$$

and

$$\Theta_\mathrm{b}(t,1)=\begin{cases}1 & \text{for top heating,}\\ 0 & \text{for bottom heating,}\\ 1 & \text{for heating from both plates.}\end{cases} \tag{13}$$

The boundary conditions for the perturbed field are

$$\Theta_\mathrm{p}=\begin{cases}u=v=0 & \text{at } y=0 \text{ or } y=1,\\ u=v=0 & \text{at } x=0 \text{ or } x=S^{-1}.\end{cases} \tag{14}$$

3. The numerical method

To simplify the computational complexity of the momentum equations, a fractional algorithm is selected. The numerical method has a first-order accuracy in the discretization of the time-dependent term, although a higher-order integration scheme has been used to deal with the intermediate velocities.

The equation of base temperature ϑ_b is first discretized with the central difference scheme in space and first-order forward difference in time. The resulting tridiagonal linear system is solved by LU decomposition. Forward and back substitutions lead the whole solution to be encoded very concisely. However, due to non-linearity, the perturbed temperature Θ_p is evaluated with an explicit scheme.

In order to describe the computational procedure more conveniently, it is defined that

$$\begin{aligned}
\frac{\partial u}{\partial t} &= F_1(u,v,p,\Theta),\\
\frac{\partial v}{\partial t} &= F_2(u,v,p,\Theta),\\
\frac{\partial \Theta}{\partial t} &= F_3(u,v,p,\Theta),
\end{aligned} \tag{15}$$

where

$$\begin{aligned}
F_1(u,v,p,\Theta) &= -u\frac{\partial u}{\partial x} - v\frac{\partial u}{\partial y} + \left(\frac{Pr}{Ra}\right)^{1/2}\nabla^2 u,\\
F_2(u,v,p,\Theta) &= -u\frac{\partial v}{\partial x} - v\frac{\partial v}{\partial y} + \left(\frac{Pr}{Ra}\right)^{1/2}\nabla^2 v + \Theta_p,\\
F_3(u,v,p,\Theta_p) &= -u\frac{\partial \Theta_p}{\partial x} - v\frac{\partial \Theta}{\partial y} + \frac{1}{\sqrt{RaPr}}\nabla^2\Theta_p.
\end{aligned} \tag{16}$$

By freezing the velocity at previous time level n and subsequently using the predictor of the fourth-order Adams scheme, one obtains

$$\begin{aligned}
\Theta_p^{n+1} = \Theta_p^n + \frac{\delta t}{24}[&55F_3(u^n,v^n,p^n,\Theta^n)\\
&- 59F_3(u^{n-1},v^{n-1},p^{n-1},\Theta^{n-1})\\
&+ 37F_3(u^{n-2},v^{n-2},p^{n-2},\Theta^{n-2})\\
&- 9F_3(u^{n-3},v^{n-3},p^{n-3},\Theta^{n-3})].
\end{aligned} \tag{17}$$

Θ_p^{n+1} is used to predict the intermediate velocity field $(\tilde{u}^{n+1},\tilde{v}^{n+1})$ with the same Adams fourth-order predictor. Θ_p should be corrected after the velocity at new time level, $n+1$, has been evaluated by the fourth-order Adams corrector, i.e.,

$$\begin{aligned}
\Theta_p^{n+1} = \Theta_p^n + \frac{\delta t}{24}[&9F_3(u^{n+1},v^{n+1},p^{n+1},\Theta^{n+1})\\
&+ 19F_3(u^n,v^n,p^n,\Theta^{n-1})\\
&- 5F_3(u^{n-1},v^{n-1},p^{n-1},\Theta^{n-2})\\
&+ F_3(u^{n-2},v^{n-2},p^{n-2},\Theta^{n-2})].
\end{aligned} \tag{18}$$

The formulations for calculating the intermediate velocities are given as

$$\begin{aligned}
\tilde{u}^{n+1} = u^n + \frac{\delta t}{24}[&55F_1(u^n,v^n,p^n,\Theta^n)\\
&- 59F_1(u^{n-1},v^{n-1},p^{n-1},\Theta^{n-1})\\
&+ 37F_1(u^{n-2},v^{n-2},p^{n-2},\Theta^{n-2})\\
&- 9F_1(u^{n-3},v^{n-3},p^{n-3},\Theta^{n-3})],\\
\tilde{v}^{n+1} = v^n + \frac{\delta t}{24}[&55F_2(u^n,v^n,p^n,\Theta^n)\\
&- 59F_2(u^{n-1},v^{n-1},p^{n-1},\Theta^{n-1})\\
&+ 37F_2(u^{n-2},v^{n-2},p^{n-2},\Theta^{n-2})\\
&- 9F_2(u^{n-3},v^{n-3},p^{n-3},\Theta^{n-3})],
\end{aligned} \tag{19}$$

where $(\tilde{u}^{n+1},\tilde{v}^{n+1})$ should be corrected with continuity equation to maintain the divergence of velocity at a given mesh lattice tending to zero. The following pressure equation also has to be solved for velocity correction,

$$\nabla^2 p = \frac{1}{\partial t}\left(\frac{\partial \tilde{u}}{\partial x} + \frac{\partial \tilde{v}}{\partial y}\right). \tag{20}$$

A conjugate-gradient algorithm Bi-CGSTAB developed by Von Der Vorst ([11]) is used. The pressure equation should satisfy a second-type homogeneous boundary condition, where the boundary is not regular and the discretized coefficient matrix for pressure may be asymmetric. The advantage of BiCGSTAB over CC (conjugate gradient) algorithm is that it not only converges more quickly, but it also maintains a smooth-converging variant. Discretizing the pressure, Eq. (20) yields

$$\mathbf{A}\vec{p} = \begin{pmatrix} a_{11} & a_{12} & \cdots & a_{1N}\\ a_{21} & a_{22} & \cdots & a_{2N}\\ \vdots & \vdots & \ddots & \vdots\\ a_{N1} & a_{N2} & \cdots & a_{NN}\end{pmatrix}\begin{pmatrix} p_1\\ p_2\\ \vdots\\ p_N\end{pmatrix} = \begin{pmatrix} d_1\\ d_2\\ \vdots\\ d_n\end{pmatrix} \tag{21}$$

where the coefficient matrix $\mathbf{A}$ is a five-diagonal matrix. The element on the main diagonal can be written as

$$a_{ii} = \frac{a_1 + a_2}{\delta x^2} + \frac{b_1 + b_2}{\delta y^2}, \tag{22}$$

with the remaining diagonal elements represented by

$$\begin{aligned}
a_{i-1i} &= -\frac{a_1}{\delta x^2} \quad a_{i+1i} = -\frac{a_2}{\delta x^2},\\
a_{ij-I} &= -\frac{b_1}{\delta y^2} \quad a_{ij+I} = -\frac{b_2}{\delta y^2},
\end{aligned} \tag{23}$$

when the total mesh number in the domain of computation is $N = I \times J$.

For the second-type homogeneous boundary conditions, the parameters are written as follows:

$$\begin{cases} a_1 = a_2 = b_1 = b_2 = 1 & \text{for lattice point not adjacent to a wall,} \\ a_1 = 0 & \text{for } \vec{n}\cdot\vec{i} = 1, \\ a_2 = 0 & \text{for } \vec{n}\cdot\vec{i} = -1, \\ b_1 = 0 & \text{for } \vec{n}\cdot\vec{j} = 1, \\ b_2 = 0 & \text{for } \vec{n}\cdot\vec{j} = -1, \end{cases} \tag{24}$$

where $\vec{n}$ is the unit normal vector of a wall surface, and $\vec{i},\vec{j}$ are, respectively, the unit vectors in the x and y directions. The pressure at $n+1$ is employed to obtain the velocity at a new time level

$$u^{n+1} = \tilde{u}^{n+1} + \delta t\left(\frac{\partial p}{\partial x}\right)^{n+1}, \qquad v^{n+1} = \tilde{v}^{n+1} + \delta t\left(\frac{\partial p}{\partial y}\right)^{n+1}. \tag{25}$$

To keep the solution physically true, the space derivatives are discretized in a staggered-mesh lattice system with the first-order upwind scheme. The choice of δt needs to fulfill the numerical stability condition; i.e., the Courant number should be less than unity.

4. Results and discussions

The computation has been carried out for Rayleigh number covering the range from 2.87×10^3 to 9.11×10^4 for the three different heating modes. The wall surface temperature difference ΔT_w and gap length L are set to be 60 K and 0.5 m, while the gap height H ranges from 0.0079 m to 0.025 m. The air in the gap has an initial temperature of 283 K, which is the same as the ambient temperature T_∞. The computational domain is partitioned to form a near-uniform space staggered grid system, while a uniform time interval δt is set in the range from 8.0×10^{-4} to 2.0×10^{-3} so that the fourth-order Adams integration scheme can be used. A preliminary four-step calculation was undertaken by the fourth-order Runge–Kutta integration scheme to provide enough data for the Adams scheme. An overall space grid number N of 100×60 was found to give grid-independent numerical results. The convergence criteria for the conjugate gradient Bi-CGSTAB scheme was chosen according to the formulation

$$\frac{\|\mathbf{A}\vec{p}-\vec{d}\|^l}{\|\mathbf{A}\vec{p}-\vec{d}\|^0} \leqslant 1.0\times10^{-6}.$$

The iteration converges after one or two iterative steps for most cases, but sometimes the convergence needs more steps, especially for the natural convection under the conditions of bottom heating and heating from both plates.

4.1. Base temperature

The dominant feature of Nusselt numbers is the base temperature field, which is independent of the horizontal coordinate with respect to the assumption of the small gap ratio S. The base temperature is governed by a transient one-dimensional diffusion equation represented by Eq. (10). Figs. 2(a)–(c) illustrate the base temperatures for three different times, i.e. $t=2.5$, 7.5, 12.5 when the Rayleigh number is 1.65×10^4. The heat-transfer rate continues to drop with time since the temperature gradient in the vicinity of the wall decreases with time monotonically. It shows that, for the top heating and bottom heating modes, the fluid motion in the region of the unheated plates may not be sensitive to the base-temperature field before $t=2.5$, as the temperature in the region is almost the same as the ambient temperature. For heating from both plates, the fluid in the gap core region has a relatively lower base temperature. The gradient of the base temperature has a significant effect on the perturbed temperature that induces the fluid motion. For the top heating case, the positive base temperature gradient seems to play a dampening role in confining the growth of the small

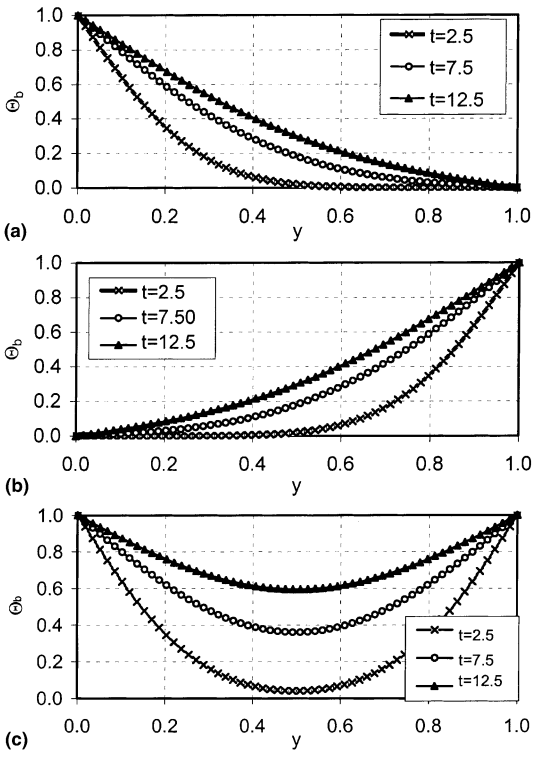

Fig. 2. The base temperature distributions in the y direction when $Ra=91\,113$ for: (a) top heating; (b) bottom heating; (c) heating from both plates.

perturbations to maintain stable flow patterns. This is similar to the effect of the viscous terms.

4.2. Average and local Nusselt numbers

For the laminar flow regime in the case of top heating, the calculated average Nusselt number, which depends mainly on the base temperature gradient near the wall, is shown in Figs. 3(a) and (b). It is found that a larger Rayleigh number leads to a relatively higher Nusselt number. Fig. 3(a) shows that the average Nusselt number during the initial stage (time less than 5) is much higher than that of the near-steady state. This means that the heat transfer through the wall surface was intensified by natural convection. After a rapid decrease, the average Nusselt number decays gradually, which seems to indicate a linear characteristic. For bottom heating and heating from both plates, the variation of average Nusselt number is almost the same as the case of top-heating mode since there is no graphical difference in the Rayleigh numbers selected. Fig. 4 shows

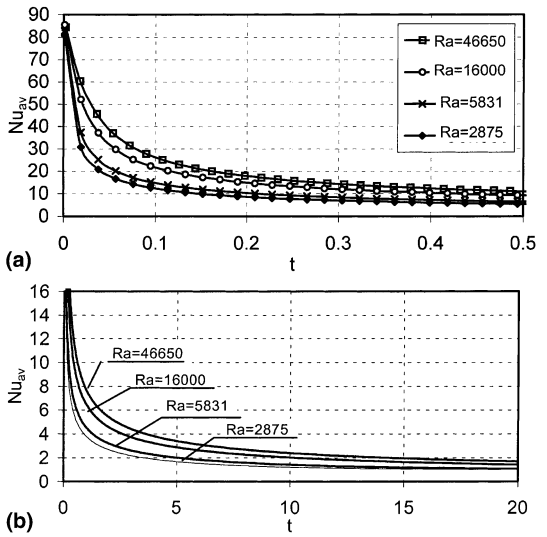

Fig. 3. Average Nusselt numbers vs time for four Rayleigh numbers.

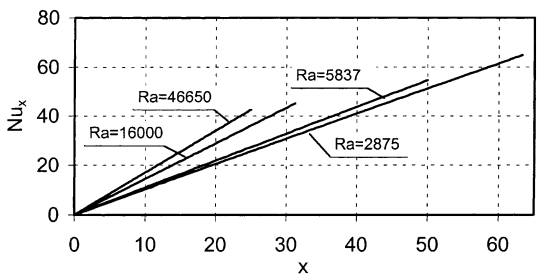

Fig. 4. Local Nusselt numbers vs x for four Rayleigh numbers.

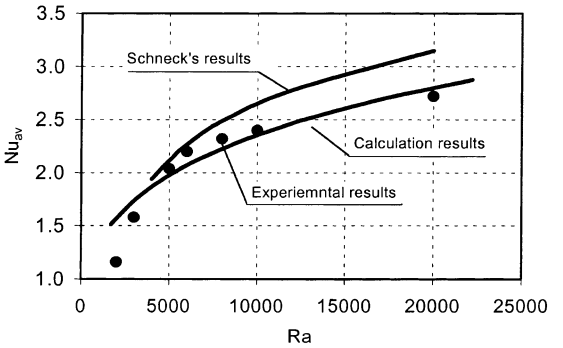

Fig. 5. Comparisons between the computational results in this paper, Rossby's experimental results and Schneck's computational results for the bottom heating case.

the relationship of the x-denoted local Nusselt number with x, linearly. It is seen that larger Rayleigh numbers cause larger local Nusselt numbers for a given x. In order to verify the computed results, the results previously reported for water natural convection [1] were used. The Prandtl number in the present computation was changed from 0.73 to 6.8 for this purpose. As shown in Fig. 5, the current curve of Nusselt numbers is very close to the curve given by Rossby, indicating that a good agreement is achieved for the bottom heating case, i.e. the Benard convection.

4.3. Thermal fluid flow properties

For different cross-sections, when x is given, the integration of its kinetic energy is defined as

$$E_{px} = \frac{1}{2}\int_0^1 (u^2 + v^2)\,\mathrm{d}y,$$

which is demonstrated in Figs. 6(a) and (b). In Fig. 6(a), for the top heating case, the distribution of the kinetic energy along x direction at time $t = 2.5$ and 5.0 with

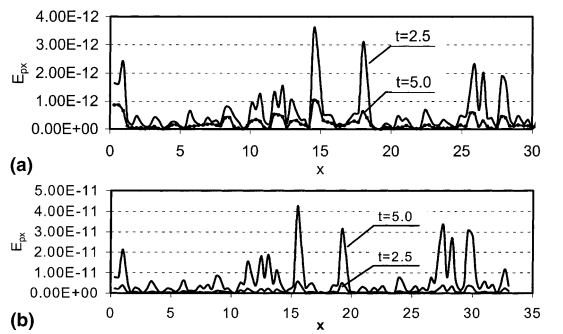

Fig. 6. Cross-sectional integration of kinetic energy in x direction for: (a) top heating for $Ra = 16\,000$; (b) bottom heating for $Ra = 19680$.

Rayleigh number $Ra = 16\,000$ is illustrated. The kinetic energy appears as a space fluctuation due to the initial temperature perturbation. This is evaluated by the multiplying series of the Gaussian random number having a deviation of unity with a small number of 10^{-5}. The thermal induced-flow kinetic energy integration has a magnitude of the order of about 10^{-12} at time $t = 2.5$, but decreases with time rapidly. By contrast, the kinetic integration grows dramatically as the time changes from $t = 2.5$ to $t = 5.0$ for the bottom heating case with Rayleigh number $Ra = 19\,680$ (see Fig. 6(b)). It is seen that fluctuating performance seems to be dependent on the initial thermal perturbation for both cases. However, the different time-changing trend for kinetic energy is intimately related to the base temperature gradient. Figs. 7(a) and (b) show the time evolution of the overall kinetic energy in the computational domain, which is defined as

$$E_{ov} = \int_0^{S^{-1}} E_p x \mathrm{d}x = \frac{1}{2} \int_0^{S^{-1}} \int_0^1 (u^2 + v^2)\, \mathrm{d}y\, \mathrm{d}x. \tag{26}$$

It is revealed that for the top heating case, the induced flow becomes stable. On the other hand, for the bottom heating case, the overall kinetic energy seems to follow an exponential trend, indicating that an initial temperature perturbation causes thermal fluid flow instability.

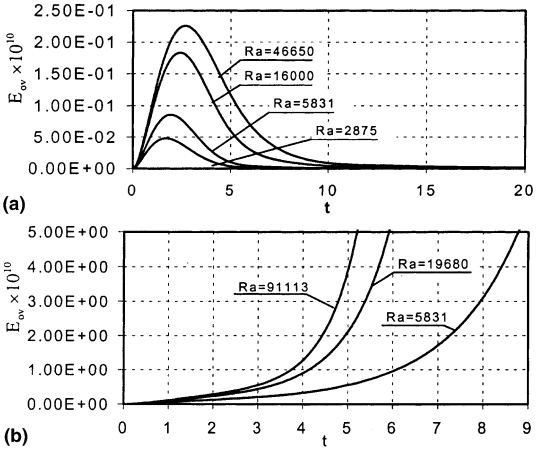

Fig. 7. The total kinetic energy for: (a) top heating; (b) bottom heating.

4.4. Perturbed flow and temperature field

Significant different fluctuating patterns can be seen from Fig. 8 for the stable and unstable thermally-induced flows. For the top heating case, when $t = 20$, the stable-heating mode makes the wavelength greater but with very small magnitudes. For the bottom-heating mode, the curves are shown in Fig. 8(b), corresponding to time $t = 15.0$. The negative base temperature leads to the perturbations fluctuating in space with short

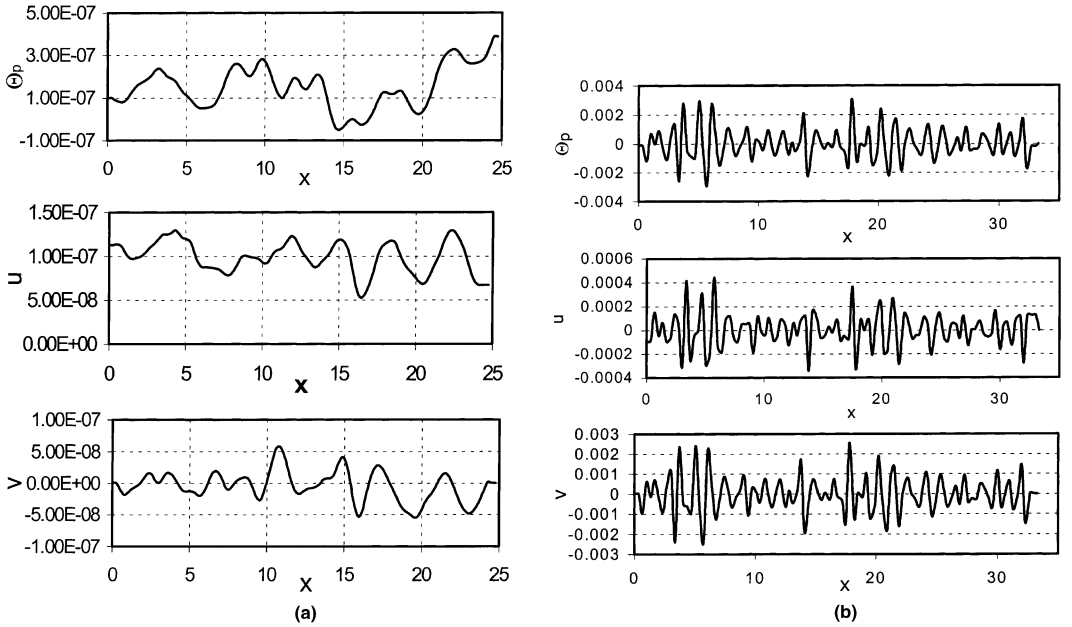

Fig. 8. (a) Distributions of perturbation variables in x direction at $y = 0.5$ for top heating when $Ra = 46\,650$; (b) distributions of perturbation variables in x direction at $y = 0.5$ for bottom heating when $Ra = 19\,680$.

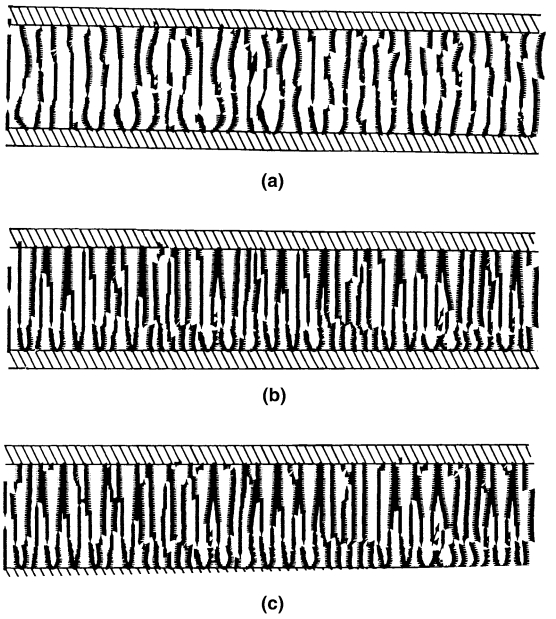

Fig. 9. Thermal fluid motions when $Ra = 91\,113$ for: (a) top heating; (b) bottom heating; (c) heating from both plates.

wavelength and quite larger magnitudes. Three different flow patterns have been illustrated in Figs. 9(a)–(c) for top heating, bottom heating and heating from both plates at time $t = 10.0$. It should be noted that although there are many rolls in the gap for the top heating case, the roll cell intensity is very small when compared with those for other cases. The energy of these roll-cell decays with time and finally the effect of initial thermal disturbance disappears. The fluctuating performance of the perturbations is closely related to these flow patterns shown in Fig. 9.

5. Conclusions

In contrast to the traditional approach of the instability study, which concentrates on solving an eigenvalue problem to obtain the neutral stability curves, a numerical method is practiced to calculate the overall perturbation kinetic energy with regard to the variation trend with time for the judgement of a flow field stability. Verification has been made for the bottom heating case by comparing average Nusselt numbers with previous numerical and experimental results. Good results are achieved for the thermally induced natural convection of water between two horizontal plates when the bottom plate is heated.

The thermal field is decomposed into two parts described by the base and perturbed temperatures. The velocity perturbation is induced purely by the temperature perturbation. Numerical study on the fractional algorithm embedding the conjugate gradient scheme Bi-CGSTAB was made to reveal the thermal fluid instability. It is found that for a small gap ratio of a channel grouped by two parallel horizontal plates, neglecting the open-ended side effect, the base temperature was governed by a transient diffusion equation. The base temperature dominates the average Nusselt number. The average Nusselt number appears to rapidly decay in the initial heating stage, and then shows almost a linear decreasing trend.

The thermal perturbation induces a flow-field fluctuation. The kinetic energy of the perturbed fluid motion shows different variation trends with time. For the top-heating mode, the overall kinetic energy finally approaches a gradually decaying stage, while for the bottom heating case, the kinetic energy seems to grow exponentially, indicating that under this heating mode, the thermal fluid motions will become unstable.

Acknowledgements

This work is financially supported by the Industrial Support Fund of the Industry Department of the Hong Kong SAR Government and the Chinese National Science Foundation with Grant No.19872062.

References

[1] P. Schneck, G. Veronis, Comparison of some recent experimental and numerical results in Benard convection, Phys. Fluids 10 (5) (1965) 927–930.
[2] L.F.A. Azevedo, E.M. Sparrow, Natural convection in open-ended inclined channels, ASME J. Heat Transfer 107 (1985) 893–901.
[3] T.S. Chen, K.L. Tzuoo, Vortex instability of free convection flow over horizontal and inclined surfaces, ASME J. Heat Transfer 104 (4) (1982) 637–643.
[4] W.W. Yousef, J.D. Tarasuk, W.J. Mckeen, Free convection heat transfer from upward-facing isothermal horizontal surface, ASME J. Heat Transfer 104 (1982) 493–499.
[5] U. Narusawa, A.Y. Suzukawa, Experimental study of double-diffusive cellular convection due to a uniform lateral heat flux, J. Fluid Mech. 113 (1981) 387–405.
[6] S. Takao, M. Tsuchiya, U. Narusawa, Numerical study of the onset of double-diffusive cellular convection due to a uniform lateral heat flux, ASME J. of Heat Transfer 104 (1982) 649–655.
[7] E.M. Sparrow, R. Ruiz, Experiments on natural convection in divergent vertical channels and correlation of divergent, convergent, and parallel-channel Nusselt numbers, Int. J. Heat Mass Transfer 31 (11) (1988) 2197–2205.
[8] K. Vafi, J. Ettefagkh, An investigation of transient three-dimensional buoyancy-driven flow and heat transfer in a closed horizontal annulus, Int. J. Heat Mass Transfers 14 (1991) 2555–2570.

[9] S.V. Iyer, K. Vafai, Passive heat transfer augmentation in a cylindrical annulus utilizing perturbations on the inner and outer cylinders, Num. Heat Transfer Part A 35 (1999) 567–586.

[10] W.L. Lin, T.F. Lin, Observation and computation of vortex and/or reverse flow development in mixed convection of air in a slightly inclined rectangular duct, ASME J. Heat Transfer 119 (1997) 691–699.

[11] H. Von Der Vorst, Bi-CGSTAB: A fast and smoothly converging variant of BICG for the solution of non-symmetric linear systems, SIAM, J. Sci. Stat. Computing 13 (1992) 631–644.